J. Fluid Mech. (2022), *vol*. 944, A1, doi:10.1017/jfm.2022.425

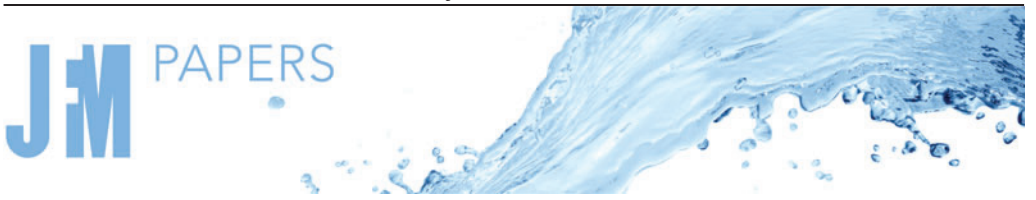

How small-scale flow structures affect the heat transport in sheared thermal convection

Guru Sreevanshu Yerragolam[1,†], Roberto Verzicco[1,2,3], Detlef Lohse[1,4] and Richard J.A.M. Stevens[1,†]

[1]Physics of Fluids Group, Max Planck Center for Complex Fluid Dynamics, J.M. Burgers Center for Fluid Dynamics, Department of Science and Technology, University of Twente, PO Box 217, 7500 AE Enschede, The Netherlands

[2]Dipartimento di Ingegneria Industriale, University of Rome 'Tor Vergata', Via del Politecnico 1, Roma 00133, Italy

[3]Gran Sasso Science Institute, Viale F. Crispi, 7, 67100 L'Aquila, Italy

[4]Max Planck Institute for Dynamics and Self-Organization, Am Fassberg 17, 37077 Göttingen, Germany

(Received 4 October 2021; revised 25 April 2022; accepted 8 May 2022)

We investigate the counter-intuitive initial decrease and subsequent increase in the Nusselt number Nu with increasing wall Reynolds number Re_w in the sheared Rayleigh–Bénard (RB) system by studying the energy spectra of convective flux and turbulent kinetic energy for Rayleigh number $Ra = 10^7$, Prandtl number $Pr = 1.0$ and inverse Richardson numbers $0 \leq 1/Ri \leq 10$. These energy spectra show two distinct high-energy regions corresponding to the large-scale superstructures in the bulk and small-scale structures in the boundary layer (BL) regions. A greater separation between these scales at the thermal BL height correlates to a higher Nu and indicates that the BLs are more turbulent. The minimum Nu, which occurs at $1/Ri = 1.0$, is accompanied by the smallest separation between the large- and small-scale structures at the thermal BL height. At $1/Ri = 1.0$, we also observe the lowest value of turbulent kinetic energy normalized with the square of friction velocity within the thermal BL. Additionally, we find that the domain size has a limited effect on the heat and momentum transfer in the sheared RB system as long as the domain can accommodate the small-scale convective structures at the thermal BL height, signifying that capturing the large-scale superstructures is not essential to obtain converged values of Nu and shear Reynolds number Re_τ. When the domain is smaller than these small-scale convective structures, the overall heat and momentum transfer reduces drastically.

Key words: turbulent convection, Bénard convection, turbulence simulation

† Email addresses for correspondence: g.s.yerragolam@utwente.nl, r.j.a.m.stevens@utwente.nl

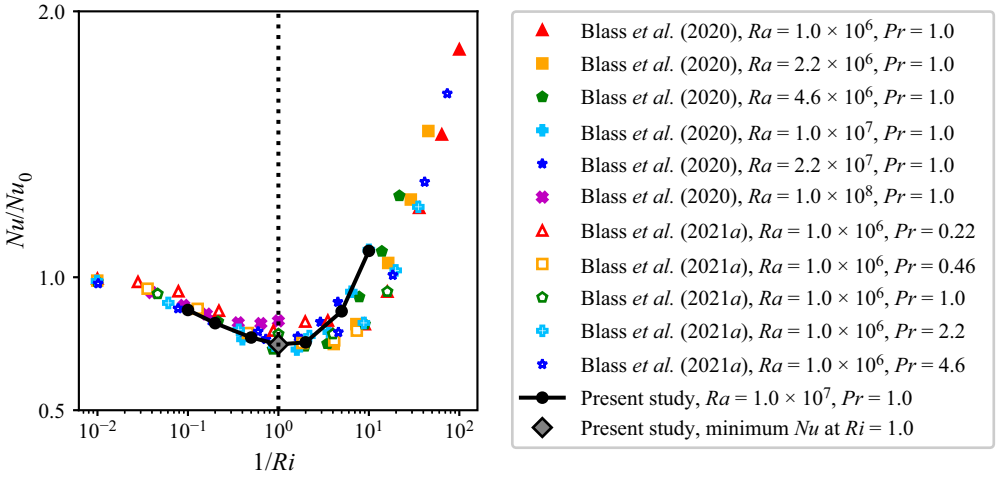

Figure 1. The ratio of Nu to Nu_0 plotted against Ri. Here Nu_0 indicates Nu for standard Rayleigh–Bénard. The grey diamond indicates the minimum Nu observed at $Ri = 1.0$ in the present simulations for $Ra = 10^7$.

1. Introduction

Sheared turbulent thermal convection is a widely occurring phenomenon in nature. It is observed in atmospheric flows (Hartmann, Moy & Fu 2001), ocean currents (Marshall & Schott 1999) and the geophysical flows present in the Earth's mantle (Richards & Engebretson 1992). Therefore, understanding the effects of shear on heat transport in turbulent flows is vital for meteorological, environmental, geophysical and industrial applications.

The sheared Rayleigh–Bénard (RB) system (Domaradzki & Metcalfe 1988; Shevkar *et al.* 2019; Blass *et al.* 2020, 2021*a*), which is obtained by adding Couette-type forcing to standard RB, is the canonical model configuration to study the interplay between buoyancy and shear in turbulent thermal convection. The properties of the fluid are indicated by the Prandtl number (Pr). The thermal driving is characterized by the Rayleigh number (Ra), while the shear driving is characterized by the wall Reynolds number (Re_w). The non-dimensional heat flux through the system is given by the Nusselt number (Nu) and the non-dimensional wall shear is given by the shear Reynolds number (Re_τ). A better control parameter to study the dependence of Nu and Re_τ on applied shear is the Richardson number ($Ri = Ra\,Pr^{-1}Re_w^{-2}$), which characterizes the ratio of the thermal to shear driving. This is because the Nu/Nu_0 data from Blass *et al.* (2020, 2021*a*) shows an appreciable collapse with $1/Ri$ for $10^6 \leq Ra \leq 10^8$, $0.22 \leq Pr \leq 4.6$ and $0 \leq Re_w \leq 10000$ as shown in figure 1. The precise definitions of these control and response parameters are mentioned in § 2.

Turbulent thermal convection is often dominated by large flow structures, which are known as turbulent superstructures (Pandey, Scheel & Schumacher 2018; Stevens *et al.* 2018). For example, such structures can be seen in cloud streets in the atmosphere (Kuo 1963), sometimes extending for hundreds of kilometres (Miura 1986). Large-scale structures have also been observed in several experiments (Ingersoll 1966; Solomon & Gollub 1990). These turbulent superstructures exhibit strong vertical coherence in RB flow (Krug, Lohse & Stevens 2020) and are thought to play a crucial role in the heat transfer of unstably stratified channel flows (Pirozzoli *et al.* 2017) and sheared RB flows (Blass, Pirozzoli & Verzicco 2019; Blass *et al.* 2020, 2021*a*). A scaling for Nu based on the 'wind

of turbulence' generated by these structures in the unstably stratified channel flows has been proposed by Scagliarini, Gylfason & Toschi (2014) along with a phenomenological model resulting in a modified logarithmic law of the wall (Scagliarini *et al.* 2015). Based on experimental observations, Shevkar *et al.* (2019) modelled the effect of wall shear on the spacing of these large-scale structures in sheared RB flow. Capturing these structures in simulations requires large computational domains. The domain size is characterized by the aspect ratios Γ_x and Γ_y, which are reported as $\Gamma_x = L_x/H$, and $\Gamma_y = L_y/H$, where L_x, L_y and H represent the streamwise, spanwise and vertical domain extent, respectively.

Various numerical studies (Bailon-Cuba, Emran & Schumacher 2010; Zhou *et al.* 2012; Chong *et al.* 2017; Stevens *et al.* 2018) have focused on understanding the effects of these large-scale structures on the heat transfer in RB flow, through restricting the domain size or through the analysis of energy spectra. These studies suggest that the heat transfer only weakly depends on the large-scale flow structures. Blass *et al.* (2021*b*) conclude that the thermal boundary layer (BL) thickness and the Reynolds number associated with the 'wind of turbulence' are very similar for simulations of $\Gamma_x = \Gamma_y = 1$ and $\Gamma_x = \Gamma_y = 32$. Observations of Stevens *et al.* (2018) suggest that although domains with aspect ratios as large as $\Gamma_x = \Gamma_y = 64$ are required to obtain convergence in the spectra of turbulent kinetic energy, the value of Nu is already converged for domains with aspect ratios of around $\Gamma_x = \Gamma_y = 4$. This suggests that the presence of superstructures is not critical for the heat transport.

Blass *et al.* (2020, 2021*a*) performed direct numerical simulations in domains of $\Gamma_x = 9\pi$, $\Gamma_y = 4\pi$ and observed that with increasing Re_w the Nu number of the sheared RB system initially decreases and subsequently increases as shown in figure 1. For strong shear, Blass *et al.* (2020) suggested that Nu scales linearly with Re_w. Analogous studies in Taylor–Couette flows have observed a scaling of $Nu \sim Re^{\gamma}$ with $\gamma \approx 0.6$ (Leng & Zhong 2021; Leng *et al.* 2021). However, the initial counter-intuitive decrease in Nu with increasing $1/Ri$ is still not very well understood. Through the visualizations of the mid-height cross-section of the temperature fields, Blass *et al.* (2020, 2021*b*) reason that the breakup of these superstructures causes the initial decrease in Nu. In standard (unsheared) RB, large-scale randomly oriented thermal superstructures dominate the flow. As shear is applied, the flow transitions from a buoyancy-dominated regime to the transitional regime where these large-scale structures break down into thin streaks. Further increasing the shear leads to reorganization of the large-scale flow structures into elongated, coherent, meandering streaks. The increase of Nu is attributed to the formation of these large-scale structures (Blass *et al.* 2020, 2021*b*). However, it is unclear whether Nu as a function of $1/Ri$ is dependent on the domain size and whether the organization of the large-scale structures has a significant impact on the heat transport in the sheared RB flow, leading us to the current study.

The manuscript is organized as follows. In § 2 we present the numerical methods used for the simulations. In § 3 we discuss the flow organization of the small-scale flow structures at the thermal BL height. In § 4 we analyse the time-averaged energy spectra of the convective heat flux and turbulent kinetic energy and in § 5 their coherence spectra. In § 6 we discuss the effect of shear on the large-scale structures. In § 7 we analyse the effect of domain size on the Nu number. Finally, conclusions are presented in § 8.

2. Numerical method

The sheared RB system is governed by the incompressible Navier–Stokes equations, the continuity equation and the transport equation for temperature, here both assumed within the Boussinesq approximation. In Cartesian coordinates $\boldsymbol{x} \equiv (x, y, z) \equiv (x_1, x_2, x_3)$, they

read as

$$\partial_t u_i + u_j \partial_j u_i = -\partial_i p + \nu \partial_j^2 u_i + \beta g \delta_{i,3} \theta, \tag{2.1}$$

$$\partial_i u_i = 0, \tag{2.2}$$

$$\partial_t \theta + u_j \partial_j \theta = \kappa \partial_j^2 \theta, \tag{2.3}$$

where $u \equiv (u_1, u_2, u_3) \equiv \left(u_x, u_y, u_z\right)$ is the velocity, $p(\boldsymbol{x}, t)$ is the kinematic pressure and $\theta(\boldsymbol{x}, t)$ the temperature with the arithmetic mean of the top and bottom wall temperatures subtracted, g is the acceleration due to gravity and β is the isobaric thermal expansion coefficient. The distance between the horizontal plates is H and the temperature difference between the plates is Δ. The top plate (at $z = H$) moves with the speed U_w, while the speed of the bottom plate (at $z = 0$) is $-U_w$. The control parameters for the system are the Rayleigh number

$$Ra \equiv \frac{\beta g H^3 \Delta}{\nu \kappa}, \tag{2.4}$$

the Prandtl number

$$Pr \equiv \nu / \kappa \tag{2.5}$$

and the wall Reynolds number

$$Re_w \equiv U_w H / \nu. \tag{2.6}$$

The non-dimensional heat flux from the hot bottom plate to the cold top plate is the Nusselt number, which has an advective and a diffusive contribution, i.e.

$$Nu \equiv \frac{\langle u_z \theta \rangle_{A,t} - \kappa \langle \partial_z \theta \rangle_{A,t}}{\kappa \Delta H^{-1}}. \tag{2.7}$$

Here, $\langle \cdots \rangle_{A,t}$ indicates the mean over time and an arbitrary horizontal plane A. Additionally, we define the friction velocity as

$$u_\tau \equiv \sqrt{\nu \langle \partial_z u_x \rangle_{w,t}}, \tag{2.8}$$

with $\langle \cdots \rangle_{w,t}$ indicating the mean over time at the top and bottom walls. The shear Reynolds number is defined as

$$Re_\tau \equiv u_\tau H / 2\nu. \tag{2.9}$$

The equations (2.1) to (2.3) are solved numerically using the AFiD GPU package (Zhu *et al.* 2018), which is based on a second-order finite-difference scheme (van der Poel *et al.* 2015). The code has been extensively validated and verified (Verzicco & Orlandi 1996; Verzicco & Camussi 1997; Stevens, Verzicco & Lohse 2010; Stevens, Lohse & Verzicco 2011; Kooij *et al.* 2018). We impose periodic boundary conditions in the horizontal directions and no-slip boundary conditions at the top and bottom plates. We use a uniform discretisation in the horizontal, periodic directions and a non-uniform grid, with a clipped Chebyshev-like clustering of nodes in the wall-normal direction. The simulations are performed for $Ra = 10^7$, $Pr = 1$ and $0 \leq Re_w \leq 10^4$ for various aspect ratios as listed in table 1.

It is ensured that the thermal BL is sufficiently resolved as per the resolution requirements put forward by Shishkina *et al.* (2010). The near-wall resolution is comparable to the values mentioned in Lozano-Durán & Jiménez (2014), Pirozzoli,

Bernardini & Orlandi (2014) and Lee & Moser (2018) to ensure that the kinetic BL is sufficiently resolved. The simulations for $\Gamma_x = 48$, $\Gamma_y = 24$ are run for 200 non-dimensional time units and flow snapshots are obtained at intervals of five non-dimensional time units from $t/t_{ff} = 100$ to $t/t_{ff} = 200$, with $t_{ff} = \sqrt{H/g\beta\Delta}$ being the free fall velocity. The energy spectra for these 21 snapshots are computed and averaged to yield the time-averaged energy spectra reported below. The *Nu* number is converged to within 1 % of its mean value, which ensures that the spectra are computed once the flow has achieved a statistically steady state.

3. Visualization of small-scale structures at thermal BL height

The *Nu* obtained from the current simulations are shown in figure 1 and agree well with the results from Blass *et al.* (2020). With increasing shear, the heat transfer initially decreases, attaining a minimum at $Ri = 1.0$, and increases again for very strong shear. We begin with a visual analysis of the instantaneous snapshots of the temperature fluctuations shown in figure 2. In agreement with Blass *et al.* (2020, 2021*a*) the snapshots at the mid-height reveal that with increasing shear, the superstructures break down from the randomly oriented convection rolls at $1/Ri = 0$ into thin elongated streaks at $1/Ri = 1.0$ for which *Nu* is lowest. Further increasing the shear leads to the formation of meandering streaks at $1/Ri = 10$. For small $1/Ri$, the flow is primarily driven by the buoyancy effects generated by the temperature field. For large values of $1/Ri$, the temperature acts more and more like a passive scalar and the flow is driven primarily by wall shear. This is reflected strongly in the large-scale flow structures. The large meandering streaks at $1/Ri = 10$ are reminiscent of the 'rollers' observed in plane Couette flow (Pirozzoli *et al.* 2014; Lee & Moser 2018).

The visualizations at the thermal BL height reveal smaller flow structures nested within the large-scale flow organization. The large-scale flow organization of the flow at the thermal BL height is similar to that at mid-height, which implies strong coherence in the vertical direction extending from mid-height to at least the thermal BL height. A visual inspection suggests that the size of the small-scale structures at the thermal BL height increases from $1/Ri = 0$ to $1/Ri = 1.0$ before it decreases again towards $1/Ri = 10$, which is confirmed later in section § 4 by studying the spectra of convective heat flux.

4. Analysis of spectra of convective flux and turbulent kinetic energy

To further analyse these smaller flow structures and their impact on the heat transfer, we compute the one-dimensional (1-D) and two-dimensional (2-D) spectra of the convective heat flux ($u_z\theta$) normalized with $U_F\Delta$ and turbulent kinetic energy (k) normalized with the square of the friction velocity u_τ. Here, $U_F = \sqrt{g\beta\Delta H}$ is the free fall velocity. These spectra are calculated at mid-height and thermal BL height as

$$\phi_{q_1,q_2}(k_x, k_y, z) = \begin{cases} \mathcal{R}\left(\mathcal{F}\left(q_1(x,y,z)\right)\mathcal{F}^*\left(q_2(x,y,z)\right)\right), & k_x \neq 0, \quad k_y \neq 0, \\ 2\mathcal{R}\left(\mathcal{F}\left(q_1(x,y,z)\right)\mathcal{F}^*\left(q_2(x,y,z)\right)\right), & k_x \neq 0, \quad k_y = 0, \\ 2\mathcal{R}\left(\mathcal{F}\left(q_1(x,y,z)\right)\mathcal{F}^*\left(q_2(x,y,z)\right)\right), & k_x = 0, \quad k_y \neq 0, \\ 4\mathcal{R}\left(\mathcal{F}\left(q_1(x,y,z)\right)\mathcal{F}^*\left(q_2(x,y,z)\right)\right), & k_x = 0, \quad k_y = 0, \end{cases} \tag{4.1}$$

where $\mathcal{R}$ represents the real value operator, $\mathcal{F}$ represents the discrete Fourier transform operator, and $\mathcal{F}^*$ represents its complex conjugate. The variables q_1, q_2 can be the convective flux ($u_z\theta$) or the turbulent kinetic energy (k). The 2-D spectra evaluated at $z = H/2$ and $z = \lambda_\theta$, corresponding to horizontal cross-sections at mid-height and the

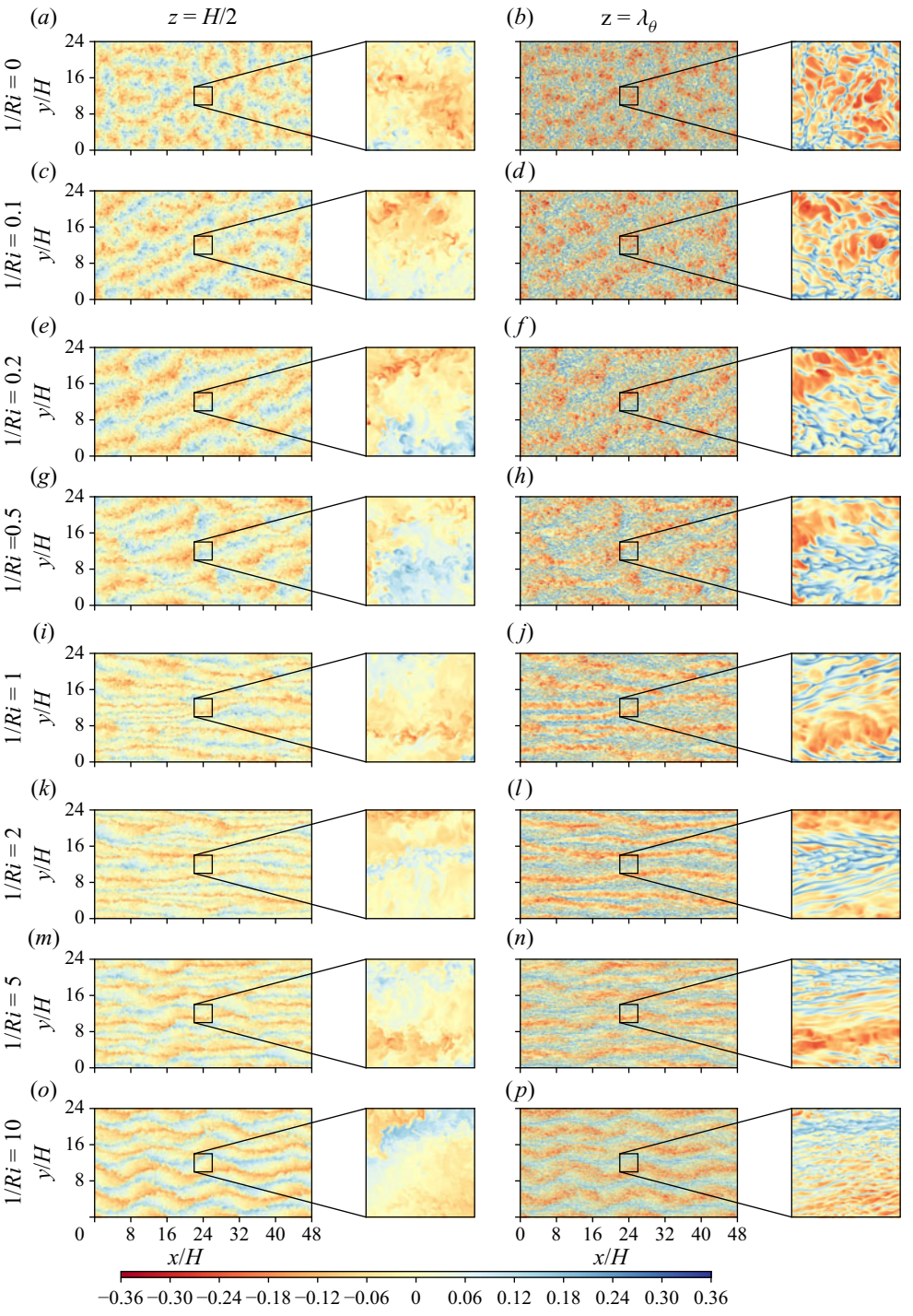

Figure 2. Visualisations of the temperature fluctuations in horizontal cross-sections. The first column is at mid-height whereas the third column is at the thermal BL height. The second and fourth columns are magnified views of the first and third column, respectively, showing the small-scale structures in greater detail.

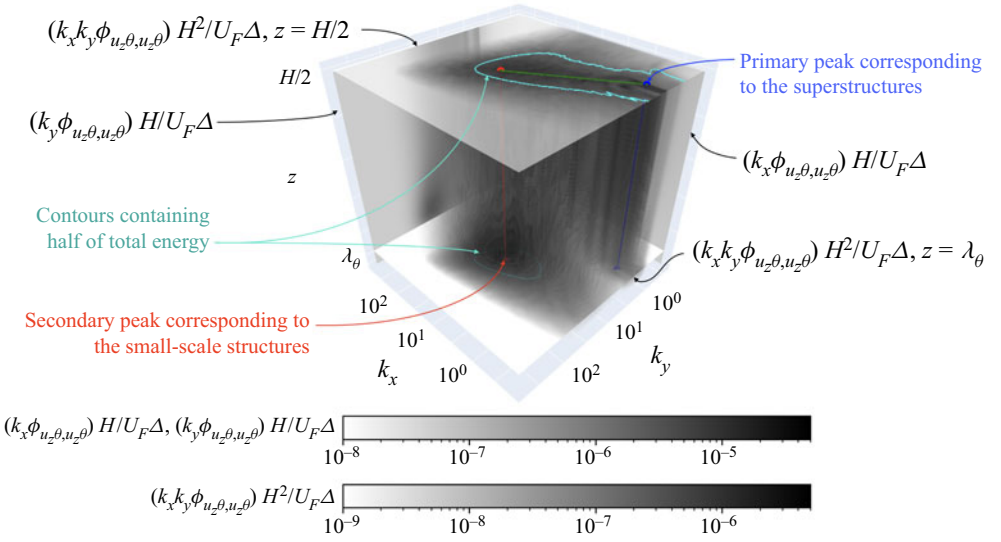

Figure 3. A 3-D representation of the premultiplied spectrum of the convective flux. The slices of normalized 2-D spectra ($(k_xk_y\phi_{u_z\theta,u_z\theta})H^2/U_F\Delta$) taken at mid-height and the thermal BL height are shown along with the normalized 1-D premultiplied spectra along the streamwise ($(k_x\phi_{u_z\theta,u_z\theta})H/U_F\Delta$) and spanwise ($(k_y\phi_{u_z\theta,u_z\theta})H/U_F\Delta$) directions. The locations of the primary and secondary peaks corresponding to the superstructures and the small-scale structures are indicated with blue and red lines, respectively. The separation between the scales is indicated with the green line. Contours containing half of the spectral energy are indicated with cyan coloured curves in these slices.

thermal BL height, respectively, are highlighted in figure 3. The 1-D spectra are obtained as

$$\phi_{q_1,q_2}(k_x, z) = \int \phi_{q_1,q_2}(k_x, k_y, z)\,\mathrm{d}k_y, \quad \phi_{q_1,q_2}(k_y, z) = \int \phi_{q_1,q_2}(k_x, k_y, z)\,\mathrm{d}k_x. \quad (4.2a,b)$$

The volume visualisation of the normalized 2-D premultiplied spectra of the convective flux $(k_xk_y\phi_{u_z\theta,u_z\theta})H^2/U_F\Delta$ for $1/Ri = 1.0$ is shown in figure 3. Two high-energy regions corresponding to the low wavenumber superstructures and high wavenumber small-scale structures are observed. Since a larger separation of scales indicates stronger turbulence, we hypothesize that the scale separation between the superstructures and small-scale structures is a measure for the turbulence inside the BLs.

Figure 4 shows the premultiplied 2-D spectra of the convective flux $(k_xk_y\phi_{u_z\theta,u_z\theta})$ computed at mid-height and the thermal BL height. The plots (i-*a*)–(viii-*a*) show two distinct high-energy regions. The coloured contours enclose half of the total spectral energy and the colours are indicative of the $1/Ri$ as they vary from red for $1/Ri = 0$ to blue for $1/Ri = 10$. The marker indicates the location of the secondary high-energy region corresponding to the small-scale structures. It is difficult to indicate a similar location for the low wavenumber high-energy region because of the lack of fully converged data. The time scales of these large-scale flow structures are very large and it is computationally very expensive to time average for a sufficient interval of time to obtain fully converged spectra in this low wavenumber region. The high-energy region at low wavenumbers corresponds to thermal superstructures, while the high-energy region at the high wavenumbers corresponds to the small-scale flow structures. As the shear imposed on

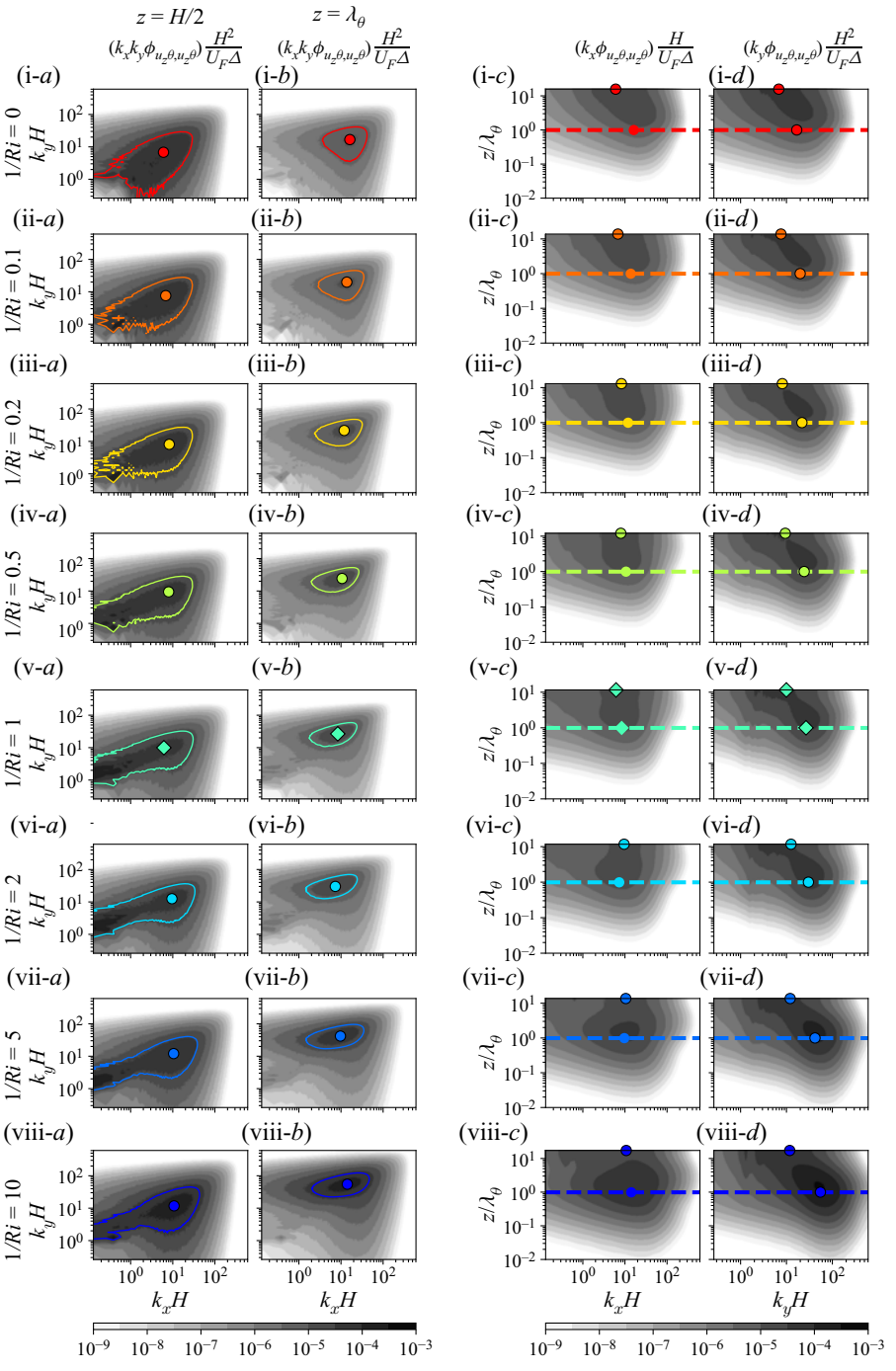

Figure 4. (i-*a*)–(viii-*b*) Two-dimensional premultiplied spectra of the convective flux. The coloured contours represent the envelope containing half of the total spectral energy. One-dimensional premultiplied spectra of the convective flux along the (i-*c*)–(viii-*c*) streamwise direction and (i-*d*)–(viii-*d*) spanwise direction. The dashed line indicates the thermal BL height. The location of the secondary peak corresponding to the small-scale structures is shown with the coloured markers. The colours of the markers and contours correspond to various $1/Ri$ as listed in the legend of figure 5.

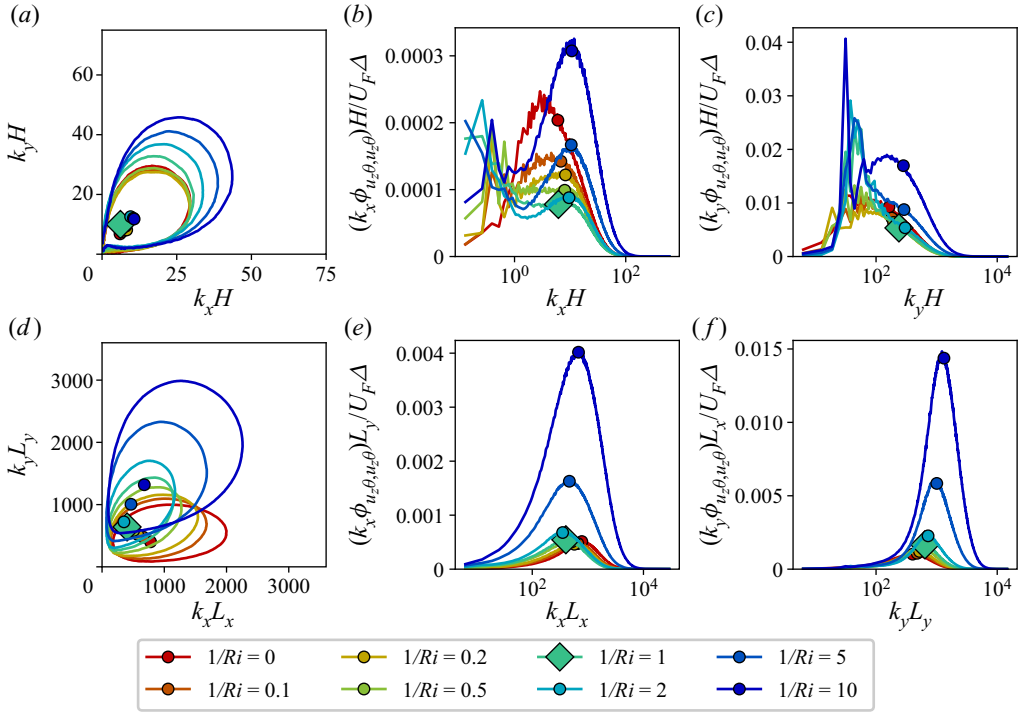

Figure 5. (*a*) Contours of normalized 2-D premultiplied convective spectra $k_xk_y\phi_{u_z\theta,u_z\theta}H^2/U_F\Delta$ taken from figure 4(i-*a*)–(viii-*a*) and (*d*) contours of normalized 2-D premultiplied convective spectra $k_xk_y\phi_{u_z\theta,u_z\theta}L_xL_y/U_F\Delta$ taken from figure 4(i-*b*)–(viii-*b*) containing half of the total spectral energy. Corresponding 1-D premultiplied spectra of the convective flux at mid-height for various $1/Ri$ plotted against the (*b*,*e*) streamwise and (*c*,*f*) spanwise wavenumber. The markers represent the location of the small-scale structure peak. Note the different scales in (*a–c*) and (*d–f*); see details in text. The location of the peaks corresponding to the superstructures is very close to the origin. Therefore, the separation between the scales of these flow structures is essentially the distance between the origin and the indicated markers.

the system increases, the separation between the superstructures and small-scale structures increases. This is demonstrated by the half-energy contours being 'stretched' more and more as $1/Ri$ increases from 0 to 10. The plots (i-*b*)–(vii-*b*) show that the secondary high-energy region is dominant at the thermal BL height. The plots (i-*c*)–(viii-*c*) and (i-*d*)–(viii-*d*) show that the secondary high-energy region occurs very close to the thermal BL height.

In order to better understand the difference in the separation between the primary and secondary peaks with increasing wall shear, we plot the half-energy contours and the location of the peaks taken from figure 4(i-*a*)–(viii-*a*) in figure 5(*a*) and we plot the half-energy contours and the location of the peaks taken from figure 4(i-*b*)–(viii-*b*) in figure 5(*b*). Although figure 5(*a*) shows that the variation with $1/Ri$ in the location of the secondary peaks at mid-height is minimal, figure 5(*d*) clearly shows that the separation of scales at the thermal BL height attains a minimum for $1/Ri = 1.0$, coinciding with the minimum in Nu shown in figure 1. Although we can not point out the exact location of the primary peaks, it is to be noted that they are very close to the origin. Therefore, the separation between the scales of these flow structures is essentially the distance between the origin and the indicated markers. Also note that the wavenumbers for figure 5(*d*) are normalized with the domain length and width while the wavenumbers for figure 5(*a*) are normalized with the domain height. For the spectra computed at the thermal BL height,

the influence of the domain size on structures is more prominent than at the mid-height due to the stronger effect of shear. Therefore, at the thermal BL height it is more useful to look at the wavenumbers normalized with the respective domain sizes rather than with the domain height. The high-energy region also shrinks in size as the shear increases from $1/Ri = 0$ to $1/Ri = 1.0$ where the secondary high-energy region is smallest. Beyond this point, the region again grows as the applied shear forcing increases from $1/Ri = 1.0$ to $1/Ri = 10.0$. A larger separation of scales in the convective flux indicates a wider range of sizes in the flow structures contributing to the heat transfer, suggesting that the thermal BL is more turbulent. The variation in the bulk is less pronounced as the bulk offers a thermal 'shortcut' at the Ra and Pr considered here (Grossmann & Lohse 2000, 2001, 2002, 2004; Stevens *et al.* 2013). Clearly, the heat flux through the BL is the bottleneck for the total heat flux through the system for the range of Ri considered here.

In addition to the separation of scales, figures 5(*b*), 5(*c*) and 5(*e*) show that the energy contained in the secondary peak shows a similar trend as Nu. With an increase in $1/Ri$, the height of the secondary peaks in figures 5(*b*), 5(*c*) and 5(*e*) initially decrease, attain a minimum for $1/Ri = 1.0$ and increase again up to $1/Ri = 10.0$. Note that the markers indicating the location of the secondary peak do not completely collapse with the location of the secondary peak in figures 5(*b*) and 5(*c*) because the marker indicates the secondary peak of the 2-D spectra as shown in figure 4. The streamwise and spanwise 1-D spectra in figures 5(*b*) and 5(*c*) are obtained by integrating the 2-D spectra from figure 4 in the spanwise and streamwise directions, respectively. The peak of the integrated 1-D spectra is at a slightly different location than the peak in the parent 2-D spectra from which it was derived. Therefore, there is a small difference in the location of the secondary peak of the 1-D and 2-D spectra; therefore, the markers in figures 5(*b*) and 5(*c*) do not always fall on the peak. This also holds true for figures 7(*b*) and 7(*c*).

Figure 6 shows the time-averaged premultiplied spectra of turbulent kinetic energy. The normalized turbulent kinetic energy represents the amount of kinetic energy contained in the turbulent fluctuations in comparison with the kinetic energy supplied through the shear forcing. At the thermal BL height, the normalized kinetic energy should be a good indicator of the effectiveness of the applied shear forcing in making the thermal BL more turbulent. In figure 6(i-*a*)–(vii-*b*) the secondary peaks are prominent and follow a similar locus of travel in the wavenumber space with variation in $1/Ri$ as the secondary energy peaks in the convective flux spectra. The variation is clearer in figures 7(*a*) and 7(*d*) with the strength of the secondary peak dominating the energy distribution at the thermal BL height as shown in figures 7(*e*) and 7(*f*).

One wonders whether for strong shear Lumley-type scaling (Lumley 1967; Lohse 1994; Biferale & Procaccia 2005) $E_u(k) \sim k^{-7/3}$ and $E_\theta(k) \sim k^{-4/3}$ for the velocity and temperature spectrum may show up in our spectra. Note that here k indicates the the wave number. However, those theoretical predictions were made for homogeneous turbulent shear flow. Given the plates, the detachment of plumes from them, and the relatively low Reynolds numbers we can numerically treat and the correspondingly short inertial range, we do not expect to see pronounced Lumley-type shear in our data. This is confirmed by the 1-D velocity and temperature spectra included in the online supplementary material available at https://doi.org/10.1017/jfm.2022.425.

5. Coherence spectra of convective flux and turbulent kinetic energy

The correlation between the heat transfer and the strength of turbulent kinetic energy can be investigated further by studying the coherence spectra between the normalized turbulent

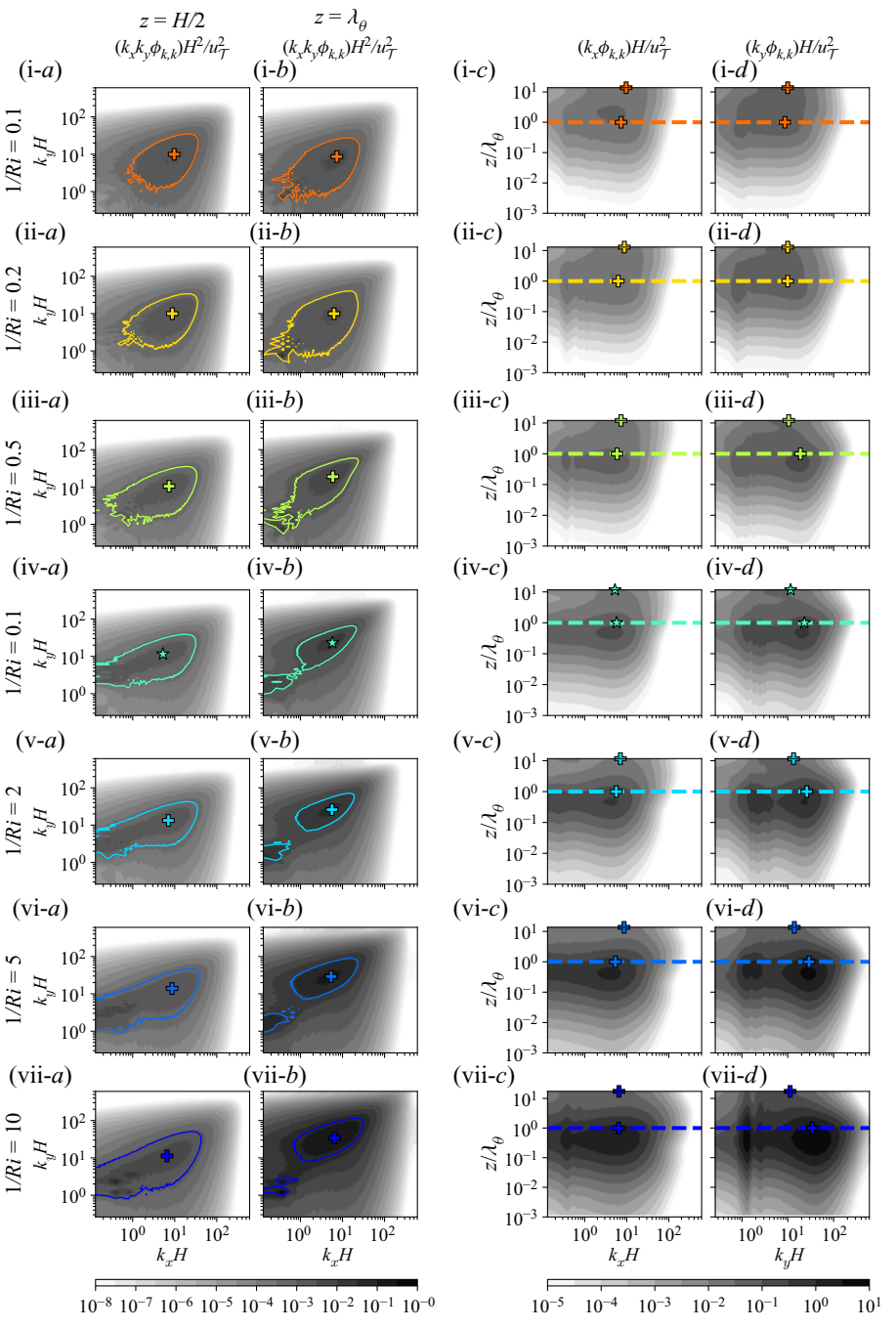

Figure 6. (i-*a*)–(viii-*b*) Two-dimensional premultiplied spectra of the normalized turbulent kinetic energy. The coloured contours represent the envelope containing half of the spectral energy. Corresponding 1-D premultiplied spectra along the (i-*c*)–(viii-*c*) streamwise and (i-*c*)–(viii-*c*) spanwise direction. The dashed line indicates the location of the thermal BL height. The location of the secondary peak corresponding to the small-scale structures is indicated by the coloured markers. The colours of the markers and contours correspond to various $1/Ri$ as listed in the legend of figure 5.

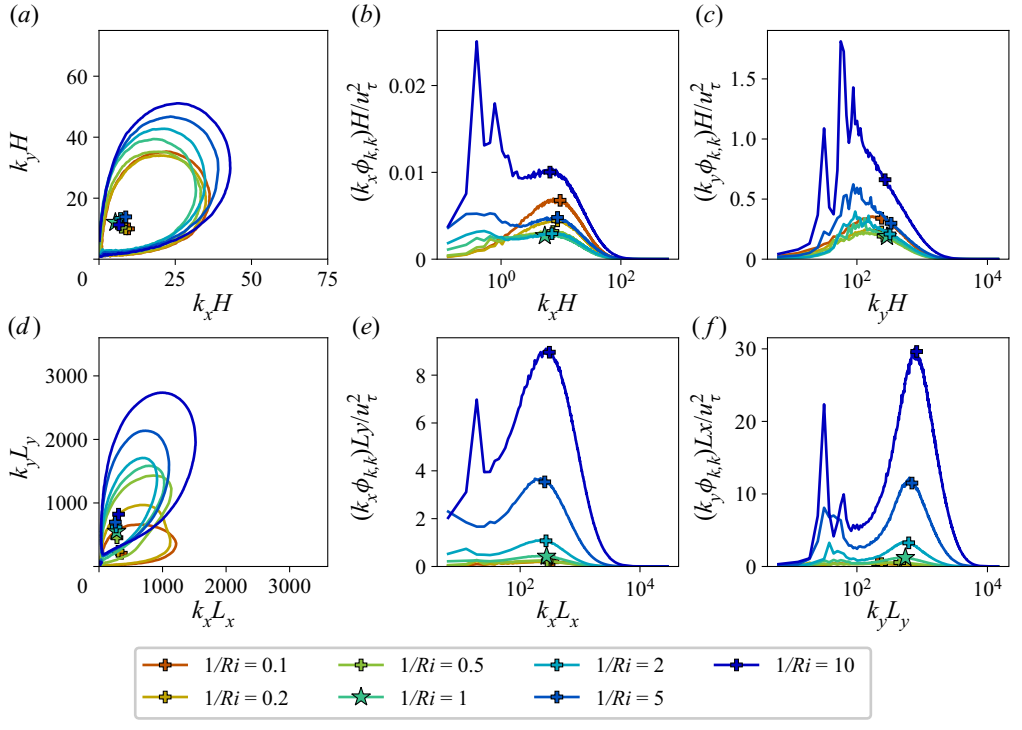

Figure 7. (*a*) Contours of normalized turbulent kinetic energy $(k_xk_y\phi_{k,k})H^2/u_\tau^2$ taken from figure 6(i-*a*)–(viii-*a*) and (*d*) contours of normalized turbulent kinetic $(k_xk_y\phi_{k,k})L_xL_y/u_\tau^2$ taken from figure 6(i-*b*)–(viii-*b*), containing half of the total spectral energy. Corresponding 1-D spectra at mid-height for various $1/Ri$ plotted against the (*b*,*e*) streamwise and (*c*,*f*) spanwise wavenumber. The markers indicate the location of the secondary peak corresponding to the small-scale structures.

kinetic energy and convective flux ($\gamma^2_{u_z\theta,k}$), which is defined as

$$\gamma^2_{u_z\theta,k}(k_x, k_y, z) = \frac{\phi_{u_z\theta,k}(k_x, k_y, z)}{\phi_{u_z\theta,u_z\theta}(k_x, k_y, z)\phi_{k,k}(k_x, k_y, z)}, \tag{5.1}$$

with $\phi_{u_z\theta,k}$ representing the co-spectra of the convective flux and turbulent kinetic energy. Figure 8(i-*a*)–(vii-*b*) shows that the wavenumbers corresponding to high-energy regions enclosing the small-scale peak of the convective flux (represented with the solid contours) are very similar to those of the turbulent kinetic energy (shown with the dotted contours). The location of the secondary peaks of the convective flux spectra (represented with the circular and diamond markers) are almost coincident with those of the turbulent kinetic energy spectra (shown with plus and star markers). The coherence between the convective flux and turbulent kinetic energy is relatively high in these regions. Figure 8(i-*c*)–(viii-*d*) shows that the coherence at the BL height is very similar for the large- and small-scale flow structures. This shows that there is a strong correlation between the turbulent kinetic energy and the convective heat flux in the BLs.

This strong correlation is also suggested by figure 9(*b*), which shows the wall-normal turbulent kinetic energy profile, averaged in time and horizontal directions and normalized with u_τ^2. It can be seen that this ratio of turbulent kinetic energy to the kinetic

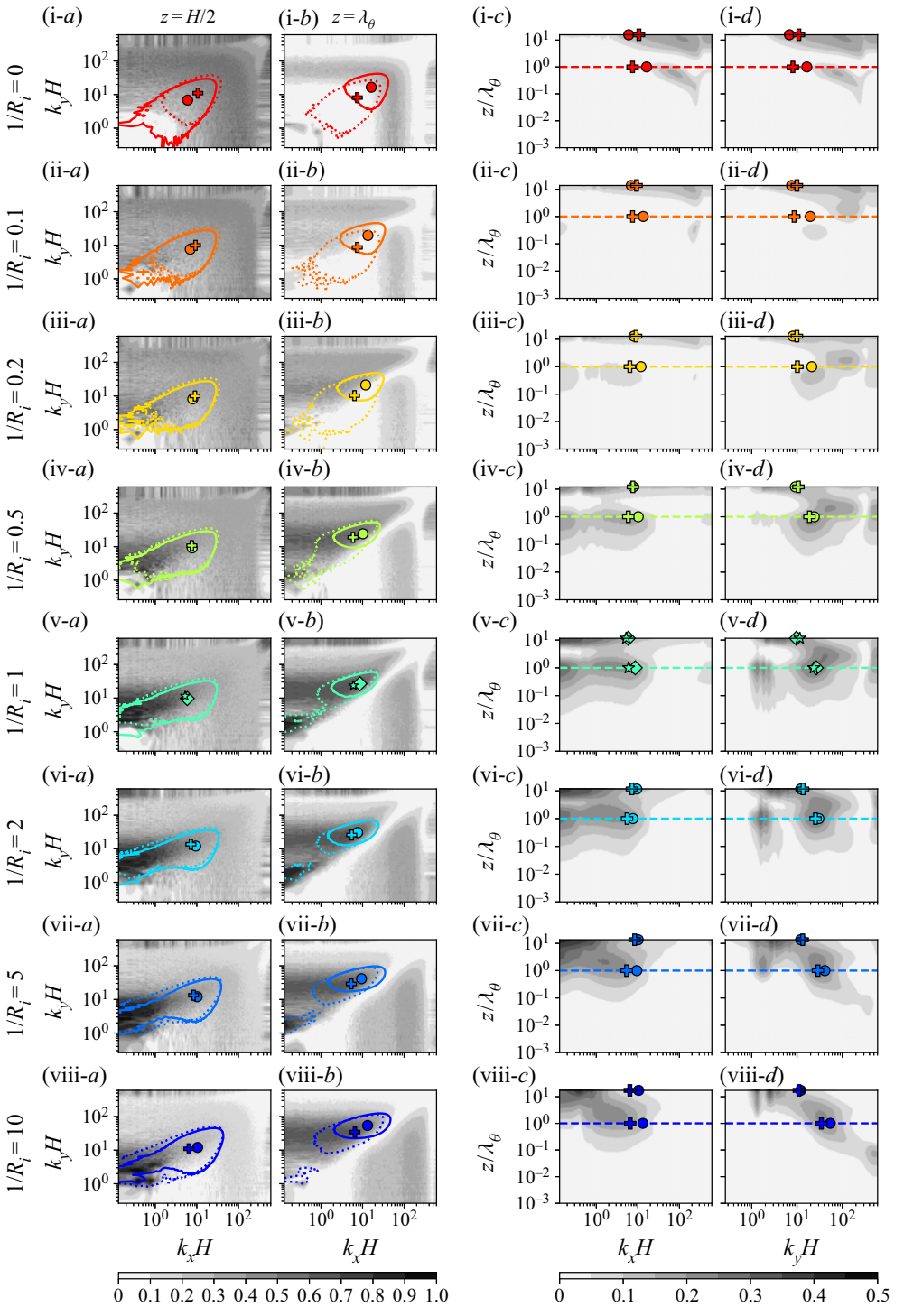

Figure 8. (i-*a*)–(viii-*b*) Coherence spectra between the convective flux and normalized turbulent kinetic energy. The dotted curve indicates the half-energy contours of the convective flux taken from figure 4(i-*a*)–(viii-*b*), and the solid curve indicates the half-energy contours of the turbulent kinetic energy taken from figure 6(i-*a*)–(viii-*b*). The markers are consistent with the legends in figures 5 and 7. Corresponding 1-D spectra along the (i-*c*)–(viii-*c*) streamwise and (i-*d*)–(viii-*d*) spanwise direction. The dashed line represents the thermal BL height.

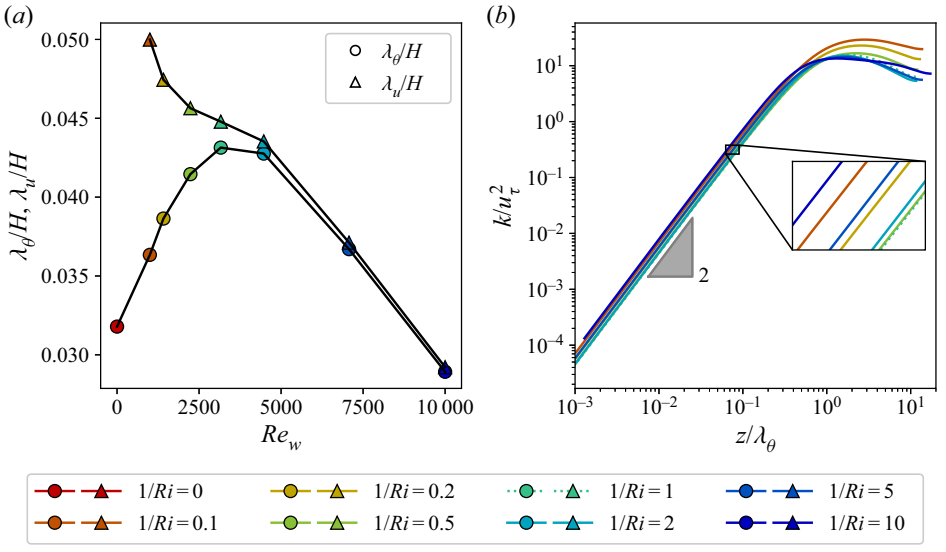

Figure 9. (*a*) Thermal BL thickness (λ_θ) and kinetic BL thickness (λ_u) vs wall Reynolds number. (*b*) The turbulent kinetic energy normalized with the square of the friction velocity plotted against wall-normal coordinate. Both plots correspond to $\Gamma_x = 48$, $\Gamma_y = 24$.

energy imparted through shear is lowest in the BL for $1/Ri = 1.0$ when Nu is lowest.

6. Effect of shear on large-scale structures

This reduction in the turbulence level in the thermal BL may be attributed to the following phenomena. The buoyancy-driven plumes responsible for the turbulent convective transport of heat are ejected from the thermal BLs (Ahlers, Grossmann & Lohse 2009) and impact the opposite BL. In sheared RB the plumes carry heat and momentum. This momentum is small for lower imposed wall velocities. In this regime, the kinetic BL is much thicker than the thermal BL, due to which the plumes carry a relatively large fraction of the momentum imposed by the wall. For higher imposed wall velocities, the kinetic BL is thinner, and the fraction of the momentum of the wall that is transferred to the plumes is relatively low. However, this is compensated by the larger wall velocity. Around $1/Ri = 1.0$, the thickness of the kinetic BL (λ_u) is only slightly larger than the thickness of the thermal BL (λ_θ) as seen in figure 9(*a*), and the wall velocity is not high enough to energize the plumes sufficiently to enhance Nu.

The change in the BL dynamics can also be observed in figure 10. Figure 10(i-*a*)–(viii-*a*) shows the probability density plot of the local horizontal flow velocity with respect to the imposed wall velocity as a function of the normalized height from the wall (z/λ_θ). Figure 10(i-*b*)–(viii-*b*) shows the corresponding plot for the local horizontal component of velocity with the temporally and spatially averaged mean subtracted. The probability densities are defined as

$$\psi_{u_x,u_y}(\alpha) = \frac{N(\alpha - \delta \leq \alpha(u_x, u_y) < \alpha + \delta)}{2N_G\delta} \quad \forall\, \alpha \in \{-\pi, -\pi + 2\delta, -\pi + 4\delta, \ldots \pi\} \tag{6.1}$$

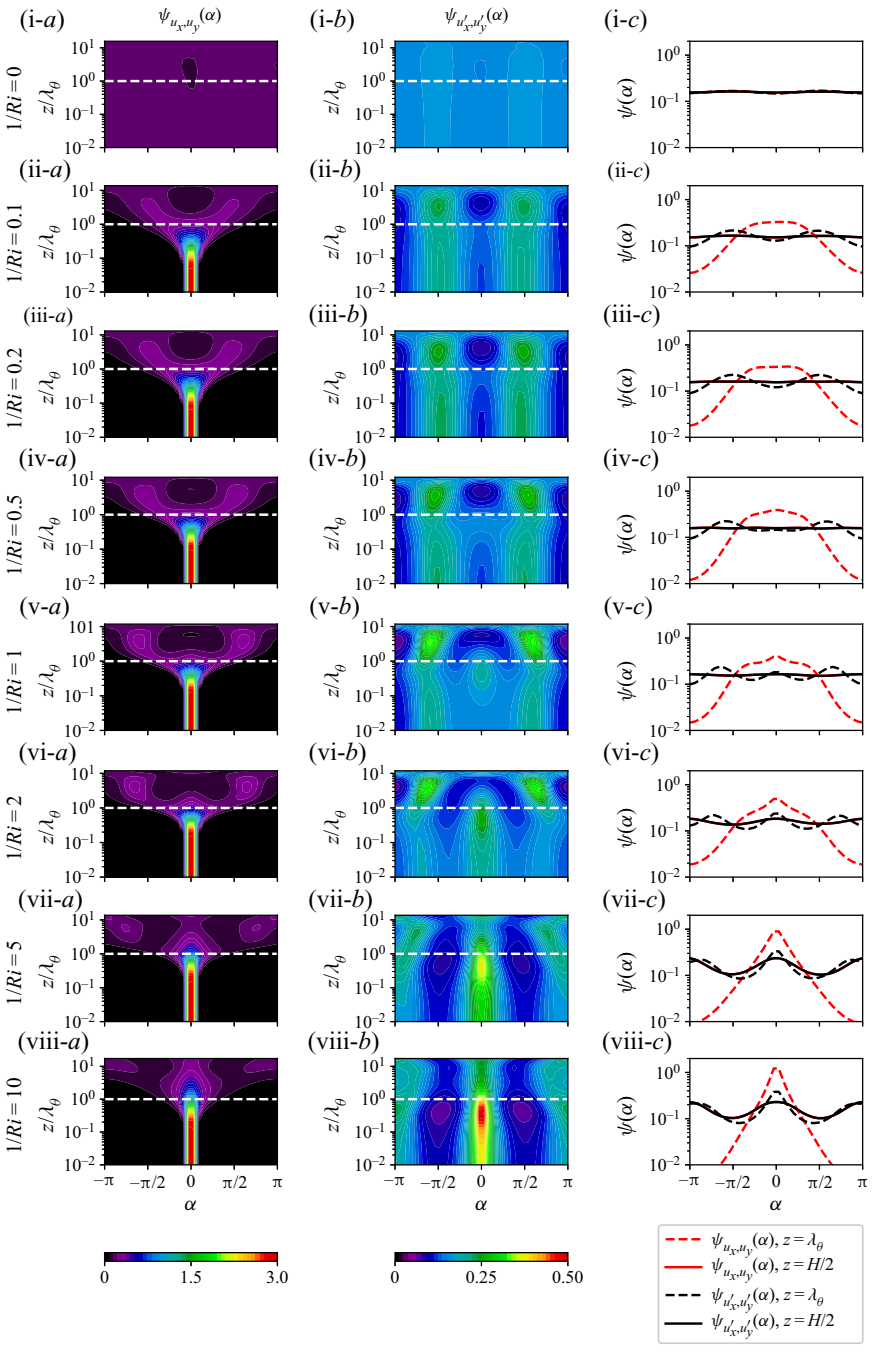

Figure 10. (i-*a*)–(viii-*a*) Probability density function given by (6.1), as a function of the angle subtended by the local horizontal component of the velocity with the streamwise direction (α), plotted against height from the wall normalized by the BL height (z/λ_θ). (i-*b*)–(viii-*b*) Probability density function of the fluctuations of the horizontal components of the velocity given by (6.2). The white dashed line indicates the thermal BL height. (i-*c*)–(viii-*c*) Probability density function of $\psi(\alpha)$ for the horizontal components and their fluctuations at mid-height and thermal BL height.

and

$$\psi_{u_x',u_y'}(\alpha) = \frac{N(\alpha - \delta \leq \alpha(u_x', u_y') < \alpha + \delta)}{2N_G\delta} \quad \forall\, \alpha \in \{-\pi, -\pi + 2\delta, -\pi + 4\delta, \dots \pi\}, \tag{6.2}$$

with $N(\cdots)$ indicating the number of grid points satisfying the condition inside the parenthesis, N_G indicating the total number of grid points at a given height z, and

$$u_x' = u_x - \langle u_x \rangle_{A,t}\,, \quad u_y' = u_y - \langle u_y \rangle_{A,t}\,. \tag{6.3a,b}$$

The angle $\alpha(u_x, u_y)$ is defined as the angle subtended by the vector $(u_x, u_y, 0)$ with $(-U_w, 0, 0)$ if the grid point under consideration lies in the bottom half of the domain. For grid points in the top half of the domain, $\alpha(u_x, u_y)$ is defined as the angle subtended by the vector $(u_x, u_y, 0)$ with $(U_w, 0, 0)$. The angle $\alpha(u_x', u_y')$ is also defined similarly. The value of δ is chosen to be $\pi/72$.

In both cases, a prominent high probability density region is observed for $\alpha \approx \pi/2$ just above the thermal BL height. This region has the highest probability density for $1/Ri = 1.0$, which shows that the velocity induced at the thermal BL height by the large-scale superstructures or plumes is primarily oriented in a direction perpendicular to that of the wall velocity, indicating that at $1/Ri = 1.0$ the imposed shear is least effective at making the thermal BLs more turbulent. A more thorough investigation involving conditional averaging of the momentum carried by the plumes, similar to the study performed in Blass *et al.* (2021*b*), could further strengthen this view. Future studies are planned to filter out the smaller scales to study the orientation of these larger heat-carrying plumes and the 'wind of turbulence' (Castaing *et al.* 1989; Grossmann & Lohse 2000) imparted by these plumes to the thermal BL.

7. Effect of domain size on Nusselt number

To further confirm that the flow structures corresponding to the secondary peaks are critical for the heat transport, we progressively reduce the domain size of the simulations to assess how this affects Nu. Figure 11 shows that the changes in the variation of Nu are minor until the domain is no longer large enough to contain the smaller flow structures associated with the secondary peak. It can be seen that a domain of aspect ratio $\Gamma_x = 1.0$, $\Gamma_y = 0.5$ is necessary to accommodate the secondary peak for most of the Ri cases considered. As soon as the domain aspect ratio is reduced to $\Gamma_x = 0.6$, $\Gamma_y = 0.3$ Nu drops drastically. Similar observations can be made on the variation of Re_τ with Re_w. As soon as the domain aspect ratio is reduced to $\Gamma_x = 0.6$, $\Gamma_y = 0.3$, we observe that Re_τ drops drastically. This observation of the minimal sheared RB domain is similar to the minimal Couette flow study performed by Sekimoto, Atkinson & Soria (2018) and the minimal channel flow study by Jiménez & Moin (1991). The minimum domain size required to obtain the Nu and Re_τ values associated with laterally unconfined sheared RB flow is a function of the shear and thermal driving. However, the fact that the domain must be sufficiently large to accommodate these small-scale structures associated with the secondary peaks is a valuable observation for reducing the computational costs of simulations focusing on the heat transport phenomena.

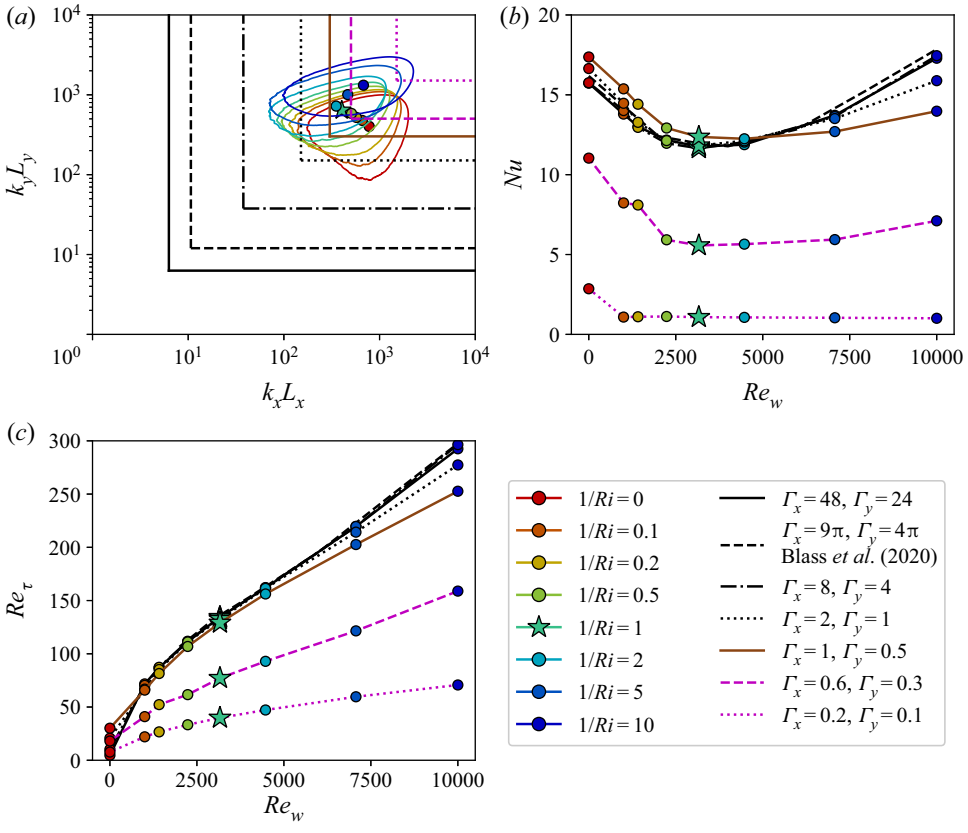

Figure 11. (*a*) Boxes showing the domain sizes overlaid on the contours from figure 5(*d*). (*b*) Plot of Nu as a function of Re_w for various domain sizes. (*c*) Plot of Re_τ as a function of Re_w for various domain sizes.

8. Conclusions

Complimentary to previous studies (Blass *et al.* 2020, 2021*a*), which focus on how the large-scale dynamics affect Nu, we focus on effects of small-scale flow structures at the BL. Since the bulk offers a thermal 'shortcut' for the range of parameters considered in the study, the BL dynamics determine the heat transfer in the system. This follows from the analysis of the spectra of convective flux and turbulent kinetic energy, which shows the presence of the spectral peaks corresponding to large-scale superstructures and small-scale structures. We observe that the separation of scales between these superstructures and small-scale structures at the thermal BL is indicative of the ratio between the turbulent kinetic energy in the thermal BL and the square of the friction velocity. A larger separation between superstructures and small-scale structures at the thermal BL height is directly correlated to a more turbulent thermal BL and a higher Nu. We also observe the minimum Nu occurs at $1/Ri = 1.0$ along with the smallest separation between superstructures and small-scale structures as well as the lowest normalized turbulent kinetic energy at the thermal BL height. The strong coherence between the small-scale structures of convective flux and turbulent kinetic energy spectra at the thermal BL height, which is similar in magnitude to that of the superstructures in the bulk, confirms that the convective heat transfer is closely related to the turbulent kinetic energy within the BLs.

Although the fluctuations of velocity in the thermal BL are imparted by the large-scale 'wind of turbulence' consisting of plumes travelling through the bulk, the orientation of these plumes impacting the BLs is determined by the momentum carried by these plumes, which, in itself, is a consequence of the BL dynamics. From probability density plots computed using (6.1), (6.2) and shown in figure 10, we observe that the momentum of the wall shear carried by the impacting plumes is lowest for $1/Ri = 1.0$, which is also the case with lowest Nu. We confirm that overall heat transfer is lowest when the applied wall shear is least effective in turning the BLs turbulent, as shown by the smallest separation between the spectral peaks of convective flux and turbulent kinetic energy at the thermal BL height for $1/Ri = 1.0$.

We find that the variation of Nu and Re_τ in sheared RB convection with domain size is limited as long as the small-scale structures associated with the secondary peaks of the convective flux and turbulent kinetic energy spectra is captured. We find that, for the parameter regime under consideration, a domain size of $\Gamma_x = 1.0$, $\Gamma_y = 0.5$ is sufficient to achieve this. We note that the identification of a minimal system size that captures the leading dynamics in sheared convection is analogous to the concept of minimal span Couette flow studies performed by Sekimoto *et al.* (2018), and the study on minimal channel flow by Jiménez & Moin (1991) which, in turn, support the inference that the large domains that fully capture the superstructures are not required to obtain the converged values of Nu and Re_τ.

Supplementary material. Supplementary material is available at https://doi.org/10.1017/jfm.2022.425.

Acknowledgements. The authors gratefully acknowledge C.S. Ng, C. Howland, A. Blass and R. Hartmann for fruitful discussions.

Funding. This work was financially supported by the ERC starting grant (2018) for the project 'UltimateRB' and the Twente Max-Planck Center. We acknowledge PRACE for awarding us access to MareNostrum at Barcelona Supercomputing Center (BSC), Spain (Project 2020225335 and 2020235589). The simulations were also supported by a grant from the Swiss National Supercomputing Centre (CSCS) under project ID s997. This work was carried out on the Dutch national e-infrastructure with the support of SURF Cooperative.

Declaration of Interests. The authors report no conflict of interest.

Author ORCIDs.
Guru Sreevanshu Yerragolam https://orcid.org/0000-0002-8928-2029;
Roberto Verzicco https://orcid.org/0000-0002-2690-9998;
Detlef Lohse https://orcid.org/0000-0003-4138-2255;
Richard J.A.M. Stevens https://orcid.org/0000-0001-6976-5704.

Appendix. Numerical simulations

https://doi.org/10.1017/jfm.2022.425 Published online by Cambridge University Press

Re_w	U_w	Ri	Γ_x	Γ_y	N_x	N_y	N_z	x^+	y^+	z_w^+	z_m^+	N_{BL}	t_{avg}/t_{ff}	$t_{avg}u_\tau/\lambda_u$	Nu	Re_τ
0.000	0.000	∞	48.0	24.0	9216	4608	256	—	—	—	—	29	100.00	—	15.73	—
1000.000	0.316	10.000	48.0	24.0	9216	4608	256	0.747	0.747	0.011	0.876	31	100.00	45.36	13.79	71.70
1414.214	0.447	5.000	48.0	24.0	9216	4608	256	0.905	0.905	0.013	1.062	32	100.00	57.89	13.01	86.85
2236.068	0.707	2.000	48.0	24.0	9216	4608	256	1.160	1.160	0.017	1.362	33	100.01	77.18	12.17	111.38
3162.278	1.000	1.000	48.0	24.0	9216	4608	256	1.400	1.400	0.020	1.643	34	100.00	94.93	11.76	134.44
4472.136	1.414	0.500	48.0	24.0	9216	4608	256	1.686	1.686	0.024	1.979	34	100.00	117.61	11.88	161.90
7071.068	2.236	0.200	48.0	24.0	9216	4608	256	2.287	2.287	0.033	2.684	31	100.00	187.10	13.71	219.60
10000.000	3.162	0.100	48.0	24.0	9216	4608	256	3.047	3.047	0.044	3.576	28	88.14	279.06	17.29	292.52
0.000	0.000	∞	8.0	4.0	1536	768	256	—	—	—	—	29	100.01	—	15.75	—
1000.000	0.316	10.000	8.0	4.0	1536	768	256	0.733	0.733	0.011	0.861	31	100.00	43.39	14.01	70.40
1414.214	0.447	5.000	8.0	4.0	1536	768	256	0.910	0.910	0.013	1.067	32	100.00	58.03	12.96	87.31
2236.068	0.707	2.000	8.0	4.0	1536	768	256	1.164	1.164	0.017	1.366	34	100.01	76.90	11.96	111.75
3162.278	1.000	1.000	8.0	4.0	1536	768	256	1.397	1.397	0.020	1.640	34	100.01	94.07	11.65	134.16
4472.136	1.414	0.500	8.0	4.0	1536	768	256	1.689	1.689	0.024	1.982	34	100.00	119.03	12.04	162.18
7071.068	2.236	0.200	8.0	4.0	1536	768	256	2.287	2.287	0.033	2.684	32	100.00	185.56	13.64	219.59
10000.000	3.162	0.100	8.0	4.0	1536	768	256	3.088	3.088	0.044	3.624	28	99.90	324.73	17.45	296.44
0.000	0.000	∞	2.0	1.0	384	192	256	—	—	—	—	29	100.00	—	16.64	—
1000.000	0.316	10.000	2.0	1.0	384	192	256	0.698	0.698	0.010	0.819	31	100.01	37.99	14.47	66.97
1414.214	0.447	5.000	2.0	1.0	384	192	256	0.889	0.889	0.013	1.043	32	100.00	55.58	13.28	85.34
2236.068	0.707	2.000	2.0	1.0	384	192	256	1.158	1.158	0.017	1.359	33	100.01	78.37	12.13	111.17
3162.278	1.000	1.000	2.0	1.0	384	192	256	1.382	1.382	0.020	1.622	34	100.00	93.38	11.82	132.66
4472.136	1.414	0.500	2.0	1.0	384	192	256	1.682	1.682	0.024	1.974	33	100.00	119.18	12.12	161.52
7071.068	2.236	0.200	2.0	1.0	384	192	256	2.233	2.233	0.032	2.620	32	100.00	176.17	13.51	214.35
10000.000	3.162	0.100	2.0	1.0	384	192	256	2.892	2.892	0.041	3.394	29	100.00	270.71	15.88	277.64

Table 1. For caption see next page.

https://doi.org/10.1017/jfm.2022.425 Published online by Cambridge University Press

Re_w	U_w	Ri	Γ_x	Γ_y	N_x	N_y	N_z	x^+	y^+	z_w^+	z_m^+	N_{BL}	t_{avg}/t_{ff}	$t_{avg}u_\tau/\lambda_u$	Nu	Re_τ
0.000	0.000	∞	1.0	0.5	192	96	256	—	—	—	—	28	300.00	—	17.37	—
1000.000	0.316	10.000	1.0	0.5	192	96	256	0.691	0.691	0.010	0.811	30	300.00	110.74	15.37	66.33
1414.214	0.447	5.000	1.0	0.5	192	96	256	0.852	0.852	0.012	1.000	31	300.00	146.78	14.41	81.78
2236.068	0.707	2.000	1.0	0.5	192	96	256	1.116	1.116	0.016	1.310	32	300.01	208.68	12.92	107.14
3162.278	1.000	1.000	1.0	0.5	192	96	256	1.347	1.347	0.019	1.581	33	300.00	259.70	12.37	129.35
4472.136	1.414	0.500	1.0	0.5	192	96	256	1.629	1.629	0.023	1.912	33	300.01	324.67	12.25	156.41
7071.068	2.236	0.200	1.0	0.5	192	96	256	2.113	2.113	0.030	2.480	33	300.00	447.89	12.70	202.84
10000.000	3.162	0.100	1.0	0.5	192	96	256	2.635	2.635	0.038	3.093	31	300.00	614.44	13.97	252.99
0.000	0.000	∞	0.6	0.3	128	128	256	—	—	—	—	29	100.00	—	16.30	—
1000.000	0.316	10.000	0.6	0.3	128	128	256	0.520	0.260	0.008	0.679	30	100.00	21.63	14.89	55.51
1414.214	0.447	5.000	0.6	0.3	128	128	256	0.703	0.351	0.011	0.917	31	100.01	37.69	13.68	74.98
2236.068	0.707	2.000	0.6	0.3	128	128	256	0.899	0.449	0.014	1.172	35	100.01	49.76	10.96	95.85
3162.278	1.000	1.000	0.6	0.3	128	128	256	1.122	0.561	0.018	1.463	36	100.00	68.53	10.73	119.66
4472.136	1.414	0.500	0.6	0.3	128	128	256	1.328	0.664	0.021	1.732	37	100.00	80.43	10.16	141.68
7071.068	2.236	0.200	0.6	0.3	128	128	256	1.746	0.873	0.028	2.277	36	100.00	115.56	10.70	186.24
10000.000	3.162	0.100	0.6	0.3	128	128	256	2.134	1.067	0.034	2.782	34	100.00	149.13	11.58	227.62
0.000	0.000	∞	0.2	0.1	64	32	256	—	—	—	—	71	100.00	—	2.86	—
1000.000	0.316	10.000	0.2	0.1	64	32	256	0.138	0.138	0.003	0.269	122	100.00	1.35	1.08	22.02
1414.214	0.447	5.000	0.2	0.1	64	32	256	0.167	0.167	0.004	0.326	121	100.00	1.69	1.10	26.65
2236.068	0.707	2.000	0.2	0.1	64	32	256	0.208	0.208	0.005	0.408	120	100.00	2.10	1.12	33.35
3162.278	1.000	1.000	0.2	0.1	64	32	256	0.249	0.249	0.006	0.487	123	100.00	2.52	1.08	39.82
4472.136	1.414	0.500	0.2	0.1	64	32	256	0.295	0.295	0.007	0.577	124	100.00	2.98	1.06	47.21
7071.068	2.236	0.200	0.2	0.1	64	32	256	0.373	0.373	0.009	0.729	125	100.00	3.79	1.04	59.62
10000.000	3.162	0.100	0.2	0.1	64	32	256	0.442	0.442	0.011	0.864	128	100.00	4.47	1.01	70.72

Table 1. Simulations considered in this work. The aspect ratio of the domain is given by Γ_x in the streamwise direction and Γ_y in the spanwise direction. The values of N_x, N_y and N_z indicate the number of grid points in the streamwise, spanwise and wall-normal directions. The grid spacing in wall units in the streamwise and spanwise directions is given by Δx^+ and Δy^+, respectively. The wall-normal grid spacing in wall units at the wall and the mid-height is given by Δz_w^+ and Δz_c^+, respectively. The number of grid points in the wall-normal direction within the thermal BL is given by N_{BL}. The values of Re_τ and Nu are averaged for the duration of the non-dimensional time given by either t_{avg}/t_{ff}, where $t_{ff} = \sqrt{H/g\beta\Delta}$ is the free fall velocity, or by $t_{avg}u_\tau/\lambda_u$.

References

Ahlers, G., Grossmann, S. & Lohse, D. 2009 Heat transfer and large scale dynamics in turbulent Rayleigh–Bénard convection. *Rev. Mod. Phys.* **81**, 503–537.

Bailon-Cuba, J., Emran, M.S. & Schumacher, J. 2010 Aspect ratio dependence of heat transfer and large-scale flow in turbulent convection. *J. Fluid Mech.* **655**, 152–173.

Biferale, L. & Procaccia, I. 2005 Anisotropy in turbulent flows and in turbulent transport. *Phys. Rep.* **414**, 43–164.

Blass, A., Pirozzoli, S. & Verzicco, R. 2019 Shear/buoyancy interaction in wall bounded turbulent flows. In *Progress in Turbulence VIII* (ed. R. Örlü, A. Talamelli, J. Peinke & M. Oberlack), pp. 47–54. Springer.

Blass, A., Tabak, P., Verzicco, R., Stevens, R.J.A.M. & Lohse, D. 2021*a* The effect of Prandtl number on turbulent sheared thermal convection. *J. Fluid Mech.* **910**, A37.

Blass, A., Verzicco, R., Lohse, D., Stevens, R.J.A.M. & Krug, D.J. 2021*b* Flow organization in laterally unconfined Rayleigh–Bénard turbulence. *J. Fluid Mech.* **906**, A26.

Blass, A., Zhu, X., Verzicco, R., Lohse, D. & Stevens, R.J.A.M. 2020 Flow organization and heat transfer in turbulent wall sheared thermal convection. *J. Fluid Mech.* **897**, A22.

Castaing, B., Gunaratne, G., Heslot, F., Kadanoff, L., Libchaber, A., Thomae, S., Wu, X.Z., Zaleski, S. & Zanetti, G. 1989 Scaling of hard thermal turbulence in Rayleigh–Bénard convection. *J. Fluid Mech.* **204**, 1–30.

Chong, K.L., Yang, Y., Huang, S. -D., Zhong, J. -Q., Stevens, R.J.A.M., Verzicco, R., Lohse, D. & Xia, K. -Q. 2017 Confined Rayleigh–Bénard, rotating Rayleigh–Bénard, and double diffusive convection: a unifying view on turbulent transport enhancement through coherent structure manipulation. *Phys. Rev. Lett.* **119**, 064501.

Domaradzki, J.A. & Metcalfe, R.W. 1988 Direct numerical simulations of the effects of shear on turbulent Rayleigh–Bénard convection. *J. Fluid Mech.* **193**, 499–531.

Grossmann, S. & Lohse, D. 2000 Scaling in thermal convection: a unifying view. *J. Fluid Mech.* **407**, 27–56.

Grossmann, S. & Lohse, D. 2001 Thermal convection for large Prandtl number. *Phys. Rev. Lett.* **86**, 3316–3319.

Grossmann, S. & Lohse, D. 2002 Prandtl and Rayleigh number dependence of the Reynolds number in turbulent thermal convection. *Phys. Rev.* E **66**, 016305.

Grossmann, S. & Lohse, D. 2004 Fluctuations in turbulent Rayleigh–Bénard convection: the role of plumes. *Phys. Fluids* **16**, 4462–4472.

Hartmann, D.L., Moy, L.A. & Fu, Q. 2001 Tropical convection and the energy balance at the top of the atmosphere. *J. Clim.* **14**, 4495–4511.

Ingersoll, A.P. 1966 Thermal convection with shear at high Rayleigh number. *J. Fluid Mech.* **25**, 209–228.

Jiménez, J. & Moin, P. 1991 The minimal flow unit in near-wall turbulence. *J. Fluid Mech.* **225**, 213–240.

Kooij, G.L., Botchev, M.A., Frederix, E.M.A., Geurts, B.J., Horn, S., Lohse, D., van der Poel, E.P., Shishkina, O., Stevens, R.J.A.M. & Verzicco, R. 2018 Comparison of computational codes for direct numerical simulations of turbulent Rayleigh–Bénard convection. *Comput. Fluids* **166**, 1–8.

Krug, D.J., Lohse, D. & Stevens, R.J.A.M. 2020 Coherence of temperature and velocity superstructures in turbulent Rayleigh–Bénard flow. *J. Fluid Mech.* **887**, A2.

Kuo, H.L. 1963 Perturbations of plane Couette flow in stratified fluid and origin of cloud streets. *Phys. Fluids* **6** (2), 195–211.

Lee, M. & Moser, R.D. 2018 Extreme-scale motions in turbulent plane Couette flows. *J. Fluid Mech.* **842**, 128–145.

Leng, X.Y., Krasnov, D., Li, B.W. & Zhong, J.Q. 2021 Flow structures and heat transport in Taylor–Couette systems with axial temperature gradient. *J. Fluid Mech.* **920**, A42.

Leng, X.Y. & Zhong, J.Q. 2021 Mutual coherent structures for heat and angular momentum transport in turbulent Taylor–Couette flows. arXiv:2111.12280.

Lohse, D. 1994 Temperature spectra in shear flow and thermal convection. *Phys. Lett.* A **196**, 70–75.

Lozano-Durán, A. & Jiménez, J. 2014 Effect of the computational domain on direct simulations of turbulent channels up to $Re_\tau = 4200$. *Phys. Fluids* **26** (1), 011702.

Lumley, J.L. 1967 Similarity and turbulent energy spectrum. *Phys. Fluids* **10**, 855–858.

Marshall, J. & Schott, F. 1999 Open-ocean convection: observations, theory, and models. *Rev. Geophys.* **37**, 1–64.

Miura, Y. 1986 Aspect ratios of longitudinal rolls and convection cells observed during cold air outbreaks. *J. Atmos. Sci.* **43** (1), 26–39.

PANDEY, A., SCHEEL, J.D. & SCHUMACHER, J. 2018 Turbulent superstructures in Rayleigh–Bénard convection. *Nat. Commun.* **9** (1), 2118.

PIROZZOLI, S., BERNARDINI, M. & ORLANDI, P. 2014 Turbulence statistics in Couette flow at high Reynolds number. *J. Fluid Mech.* **758**, 327–343.

PIROZZOLI, S., BERNARDINI, M., VERZICCO, R. & ORLANDI, P. 2017 Mixed convection in turbulent channels with unstable stratification. *J. Fluid Mech.* **821**, 482–516.

VAN DER POEL, E.P., OSTILLA-MÓNICO, R., DONNERS, J. & VERZICCO, R. 2015 A pencil distributed finite difference code for strongly turbulent wall-bounded flows. *Comput. Fluids* **116**, 10–16.

RICHARDS, M.A. & ENGEBRETSON, D.C. 1992 Large-scale mantle convection and the history of subduction. *Nature* **355** (6359), 437–440.

SCAGLIARINI, A., EINARSSON, H., GYLFASON, A. & TOSCHI, F. 2015 Law of the wall in an unstably stratified turbulent channel flow. *J. Fluid Mech.* **781**, R5.

SCAGLIARINI, A., GYLFASON, A. & TOSCHI, F. 2014 Heat-flux scaling in turbulent Rayleigh–Bénard convection with an imposed longitudinal wind. *Phys. Rev.* E **89**, 043012.

SEKIMOTO, A., ATKINSON, C. & SORIA, J. 2018 Characterisation of minimal-span plane Couette turbulence with pressure gradients. *J. Phys.: Conf. Ser.* **1001** (1), 012020.

SHEVKAR, P.P., GUNASEGARANE, G.S., MOHANAN, S.K. & PUTHENVEETIIL, B.A. 2019 Effect of shear on coherent structures in turbulent convection. *Phys. Rev. Fluids* **4**, 043502.

SHISHKINA, O., STEVENS, R.J.A.M., GROSSMANN, S. & LOHSE, D. 2010 Boundary layer structure in turbulent thermal convection and its consequences for the required numerical resolution. *New J. Phys.* **12**, 075022.

SOLOMON, T.H. & GOLLUB, J.P. 1990 Sheared boundary layers in turbulent Rayleigh–Bénard convection. *Phys. Rev. Lett.* **64**, 2382–2385.

STEVENS, R.J.A.M., BLASS, A., ZHU, X., VERZICCO, R. & LOHSE, D. 2018 Turbulent thermal superstructures in Rayleigh–Bénard convection. *Phys. Rev. Fluids* **3**, 041501(R).

STEVENS, R.J.A.M., LOHSE, D. & VERZICCO, R. 2011 Prandtl and Rayleigh number dependence of heat transport in high Rayleigh number thermal convection. *J. Fluid Mech.* **688**, 31–43.

STEVENS, R.J.A.M., VAN DER POEL, E.P., GROSSMANN, S. & LOHSE, D. 2013 The unifying theory of scaling in thermal convection: the updated prefactors. *J. Fluid Mech.* **730**, 295–308.

STEVENS, R.J.A.M., VERZICCO, R. & LOHSE, D. 2010 Radial boundary layer structure and Nusselt number in Rayleigh–Bénard convection. *J. Fluid Mech.* **643**, 495–507.

VERZICCO, R. & CAMUSSI, R. 1997 Transitional regimes of low-Prandtl thermal convection in a cylindrical cell. *Phys. Fluids* **9**, 1287–1295.

VERZICCO, R. & ORLANDI, P. 1996 A finite-difference scheme for three-dimensional incompressible flow in cylindrical coordinates. *J. Comput. Phys.* **123**, 402–413.

ZHOU, Q., LIU, B.-F., LI, C.-M. & ZHONG, B.-C. 2012 Aspect ratio dependence of heat transport by turbulent Rayleigh–Bénard convection in rectangular cells. *J. Fluid Mech.* **710**, 260–276.

ZHU, X., *et al.* 2018 AFiD-GPU: a versatile Navier–Stokes solver for wall-bounded turbulent flows on GPU clusters. *Comput. Phys. Commun.* **229**, 199–210.